Effect of Artificial Large-scale Structures on Bursting Phenomenon in Turbulent Boundary Layer

Xiaonan Chen (陈晓楠),[1] Koji Iwano (岩野　耕治),[1,a)] Yasuhiko Sakai (酒井　康彦),[2] and Yasumasa Ito (伊藤　靖仁)[1]

[1)] *Department of Mechanical Systems Engineering, Nagoya University, Nagoya 464-8603, Japan*

[2)] *Nagoya Industrial Science Research Institute, Nagoya 464-0819, Japan*

(Dated: 21 July 2022)

In this study, the effect of artificial very-large-scale motions (AVLSMs) generated by a dielectric-barrier-discharge plasma actuator (DBD-PA) array on the bursting phenomenon in the near-wall region ($y^+ \leq 40$ in the present study) was experimentally investigated. The DBD-PA array was embedded in the wall where the turbulent boundary layer (TBL) was fully developed. A hot-wire rake consisting of nine I-type probes was used to measure the streamwise fluctuation velocity throughout the TBL at two positions downstream from the DBD-PA array. At both measurement positions in the streamwise direction, it was observed that the negative artificial very-large-scale motions (nAVLSM) flanked on two sides by positive motions (pAVLSM) could extend to above 0.3δ height from the wall. The bursting phenomenon was detected using the variable-interval time-averaging technique. It was observed that the bursting phenomenon in pAVLSM was suppressed, whereas it was enhanced in nAVLSM. Further investigation showed that the bursting frequency normalized by the inner variables in nAVLSMs is the same as that of pAVLSMs only at the secondary measurement position, which is far from the DBD-PA array. These results suggest that the quasi-steady quasi-homogeneous (QSQH) theory only holds when the TBL is sufficiently developed.

[a)] Electronic mail: iwano@nagoya-u.jp

I. INTRODUCTION

In the turbulent boundary layer (TBL), the bursting phenomenon has attracted the most attention over the last several decades, because this process is strikingly violent and produces the most turbulent kinetic energy. As observed by Kline *et al*.[1], the bursting phenomenon can be explained as a near-wall low-speed streak lifted away from the wall by an accompanying quasi-streamwise vortex (QSV). The lift-up of the low-speed streak (namely "ejection") is usually followed by a "sweep" event, which refers to the entry of a high-speed fluid from upstream[2]. Further investigation has shown that ejection events (termed to as 'bursts' in Lu & Willmarth (1973)) account for 77% of the Reynolds stress throughout the TBL, whereas sweep events provide 55%. Notably, the total Reynolds stress provided by ejection and sweep exceeds 100% because other motion types provide an opposite Reynolds stress[3]. Reynolds stress is primarily important for skin friction[4]. As estimated by Airbus, for one airplane (A320 type), even a 1% drag reduction is expected to reduce the annual operating costs substantially[5]. Therefore, controlling the TBL and suppressing the near-wall bursting phenomenon to reduce skin friction are of great engineering and economic interest.

In recent years, attention has shifted from the near-wall to the logarithmic region, where a secondary peak was found in the pre-multiplied power spectra of the streamwise fluctuation velocity in the high-Reynolds-number case[6]. A secondary peak exists at a large wavelength, suggesting that large-scale structures contribute the most to turbulent production in the logarithmic region[7–9]. These large-scale structures include large-scale motions (LSMs)[10], very-large-scale motions (VLSMs)[11], and large-scale streamwise vortices flanked on one side or symmetrically on the two sides of the LSMs[12–14]. These natural LSMs and VLSMs have been proven to have a significant modulation effect on near-wall fluctuation velocity signals[15–19]. To demonstrate the modulation effect of natural large-scale structures, the quasi-steady quasi-homogeneous (QSQH) theory has suggested that the friction velocity fluctuates in unison with large-scale structures, i.e., the local friction velocity increases when positive structures exist and decreases when negative structures appear, by which the large-scale structures modulate the amplitude and frequency of the near-wall streamwise fluctuation velocity signal[20–22]. A further study by Chen *et al*.[23] found that the bursting phenomenon frequency normalized by the local inner variables was the same for different types of large-scale structures, which provides experimental support for the QSQH theory. However, the applicability of QSQH theory to artificial very-large-scale motion (AVLSM) has never been examined.

In the present study, we aimed to investigate the effect of AVLSMs on the near-wall bursting phenomenon. If the QSQH theory still works in a modified wall-bounded turbulent fluid flow case, the bursting frequency under different AVLSMs should remain constant when normalized by the local friction velocity. In this case, the bursting frequency will increase under positive AVLSMs (pAVLSMs) and decrease under negative AVLSMs (nAVLSMs) because the friction increases under pAVLSMs and decreases under nAVLSMs. However, if the QSQH theory fails, the investigation results may provide new insights into the suppression of the near-wall bursting phenomenon.

To control the structures in TBL, both passive and active flow control methods have proven useful. For example, in the passive flow control case, Kevin *et al*.[24] used a herringbone-patterned riblet surface to induce large-scale motion at a fixed position on a plate in TBL. For the active flow control case, Tang *et al*.[25] found that the synthetic input of a piezoelectric actuator can affect the amplitude modulation effects in TBL. Their further investigation indicates that the piezoelectric actuator can reorganize the near-wall small-scale intermittent bursting events[26]. Cheng *et al*.[27] used a plasma actuator array to create large-scale streamwise vortices (LSSVs) to stabilize the near-wall low-speed streak and subsequently suppress the near-wall bursting phenomenon in a TBL. Owing to the external energy injection, the active control approach is expected to achieve a more effective result in creating AVLSMs and suppressing the bursting phenomenon than the passive ones. Therefore, in the present study, we decided to create AVLSMs using a dielectric barrier discharge plasma actuator (DBD-PA) array, which is easy to fabricate and embed in the wall. Although the DBD-PA used in the present study is similar to that used by Cheng *et al*.[27], the approach for suppressing the bursting phenomenon is different. The artificial LSSVs created by Cheng *et al*.[27] have a size comparable to the near-wall low-speed streak, and therefore were used to directly control the near-wall bursting phenomenon. However, the AVLSMs created to examine the QSQH theory in the present study must have a much larger scale than the near-wall bursting-related structures and therefore were expected to last longer in the streamwise direction and affect the bursting phenomenon in a larger area.

II. EXPERIMENTAL APPARATUS AND CONDITIONS

The experiment was performed in a blowout type boundary layer wind tunnel (Eiffel-type). The test section had a length of 2600 mm and a width of 520 mm. The TBL in the present study was developed on a flat plate. To reduce heat loss from the hot-wire when recording fluctuation velocity signal near the wall surface, the flat plate used in the experiment is a Bakelite plate with low thermal conductivity. The plate sized 2100 mm in length, 520 mm in width, and 8 mm in thickness. To avoid disrupting the flow, the tip of the flat plate was modified into a parabolic shape. A 1.0 mm diameter tripping wire was installed 50 mm downstream from the leading edge to promote the transition to turbulent flow. Throughout the present study, we use x, y, and z to refer to the streamwise, wall-normal, and spanwise directions, respectively. The variables normalized by the inner scale, i.e., kinematic viscosity ν and friction velocity u_τ, are denoted by superscript +.

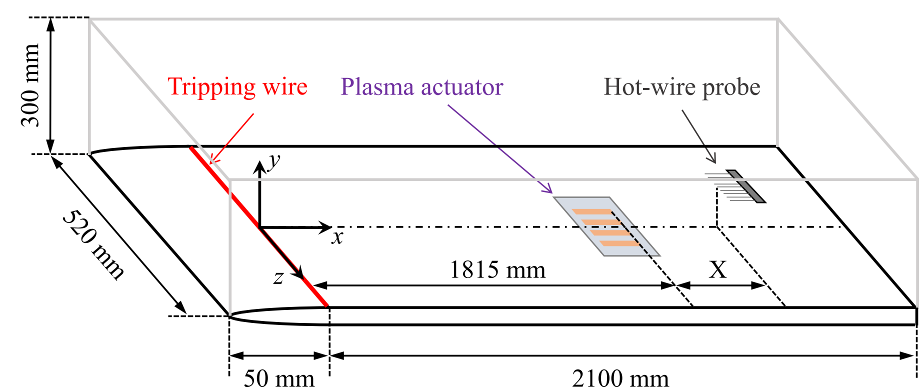

FIG. 1. The schematic of the test section.

In order to create the AVLSMs, a spanwise DBD-PA array shown in Fig.2 was adopted in the present study. The DBD-PA is constructed by a dielectric sandwiched between two electrodes in a specific arrangement as shown in Fig.3. When a high voltage, high frequency alternating current (AC) power is supplied to the two electrodes of the DBD-PA, the air near the electrodes will be ionized and accelerated by the electric field between the electrodes, creating an ionic wind. The ionic wind collides with neutral particles and then generates a jet away from the exposed electrode[28–30]. The DBD-PA array module is embedded at $x = 1,730$ mm to $x = 1,830$ mm as shown in the schematic of test section, i.e., Fig.1. The dimensions of the DBD-PA array is shown in Fig.3. The quartz glass plate used as dielectric is 0.5 mm thick and its top surface is in the same plane with the wall of the turbulent boundary layer. Copper foil tape with a thickness of 0.07 mm was used as the electrode.

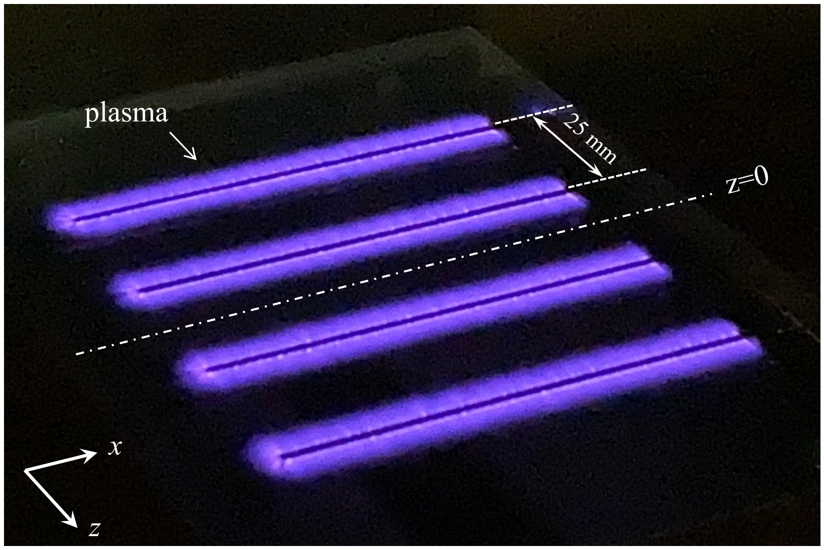

FIG. 2. DBD-PA array used in the experiment.

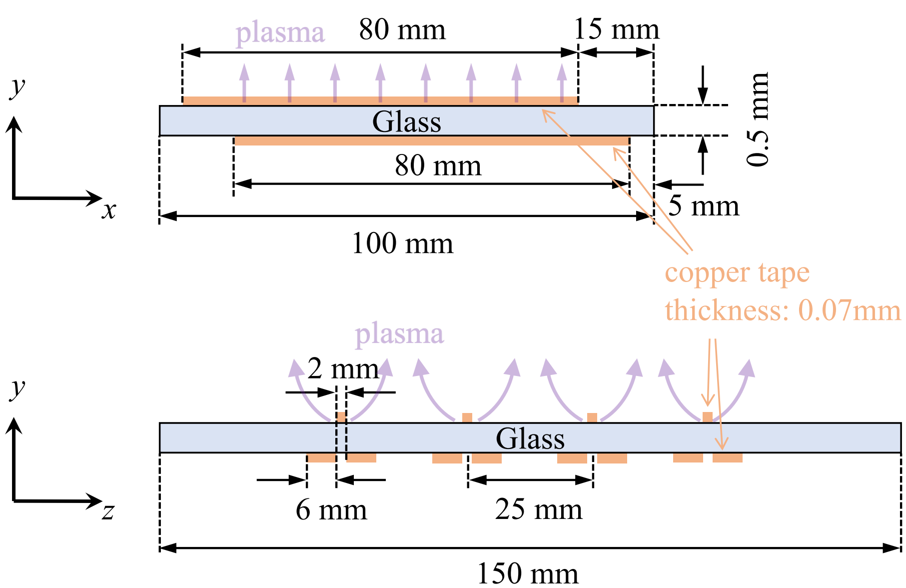

FIG. 3. Schematic of the DBD-PA array module used in the experiment.

The freestream velocity U_∞ was approximately 11 m/s with a turbulent intensity of 0.4%. The measurement equipment was a hand-made hot-wire rake (Fig.4) operated by the hand-made constant temperature anemometer circuits[23]. The roll-off frequency of the anemometer system estimated by a sine wave test was 10 kHz. The hot-wire rake comprised nine I-type hot-wire probes with 4 mm spacing which are numbered from 1 to 9 as shown in Fig.4. The viscous scaled length of the hot-wire was $l^+ = u_\tau l/\nu = 15$, and the length to diameter ratio was $l/d = 200$, suggesting that the hot-wire probe used in the present study has the ability to capture the smallest fluctuation of the streamwise velocity in the TBL[31]. To investigate the flow field modified by the DBD-PA array, the streamwise fluctuation velocities of 69 points ranging from $y = 0.16$ mm to $y = 79.96$ mm at two streamwise positions were measured by the rake. The first position in the x-direction was set to $x = 1,855$ mm (denoted by "L1"), while the second position in the x-direction was $x = 1,895$ mm (denoted by "L2"), so that the distance between the rake and the downstream edge of the upper electrodes of the DBD-PA was approximately $X/\delta = 1$ and $X/\delta = 2$, respectively. Here, X is the streamwise distance between the hot-wire rake and the downstream edge of the upper electrodes of the DBD-PA as shown in Fig.1. δ is the boundary layer thickness. At both streamwise positions, the boundary layer thickness was about $\delta = 39.9$ mm, at which wall-normal distance the mean streamwise velocity is 99.5% of the freestream velocity. The friction velocity was approximately $u_\tau = 0.45$ m/s, and the Reynolds number based on the friction velocity was $Re_\tau = u_\tau \delta/\nu = 1,170$. At all measurement positions, the streamwise fluctuation velocities were measured in two conditions. In the one, DBD-PA was turned on (denoted by "PAON"), while in the other, DBD-PA was turned off (denoted by "PAOFF"). In each case, at each position, the friction velocity was estimated for each probe individually. The normalized data of each position in each case shown in the paper was normalized by u_τ estimated at the same position of the same case. The measurement data were recorded by a 16-bit A/D converter. The sampling frequency was 20 kHz and the sampling number was 262,144 (about 13.1 s). The DBD-PA array was operated by a square-wave voltage signal with an amplitude of 6.0 kV, and a frequency of 5.0 kHz generated by a high voltage/frequency power supply (PSI-PG1040F, KI-tech).

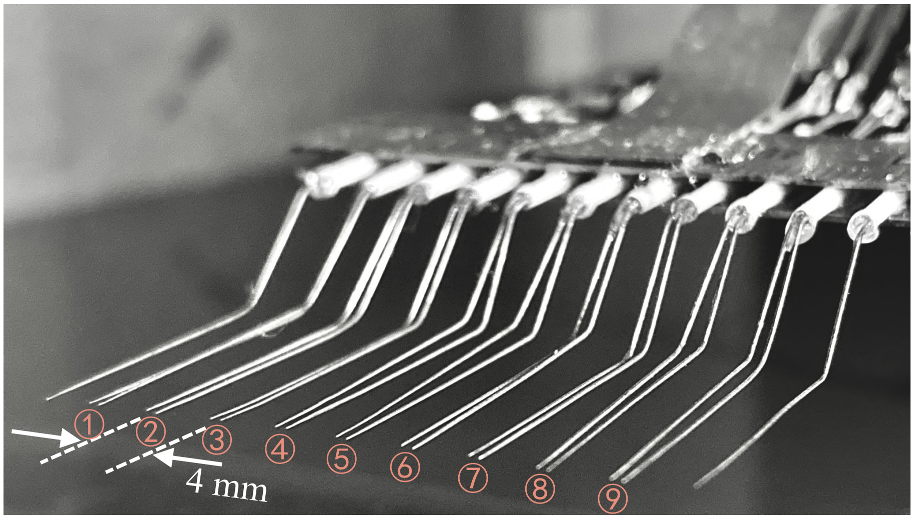

FIG. 4. Multi-channel hot-wire probe used in the experiment.

The mean streamwise velocity and the root-mean-square (RMS) streamwise velocity measured by the rake at $X/\delta = 1$ when the DBD-PA array was turned off, are shown in Fig.5 and Fig.6, respectively. Since similar results have been confirmed, the results measured at $X/\delta = 2$ under the same condition will not be shown here. The height of each probe in wall-normal direction and the friction velocity were estimated by fitting the mean velocity with the Musker profile[32] given by Eq.(1) within a range of $0 < y^+ \leq 100$. Specifically, the cumulative errors between the inner-variables normalized mean velocity profile measured in the experiment and the Musker profile were calculated. The height of the probe and the friction velocity u_τ were estimated by choosing the values with which the minimum value of cumulative errors was obtained. The constants used in the Musker profile were the same with Musker[32], i.e., $\kappa = 0.41$ and $s = 1.093 \times 10^{-3}$. Both the mean velocity and the turbulent intensity measured by each probe in rake fit well with each other. The mean velocity profile also fits well with the one measured by Degraaff & Eaton[33] in a fully developed turbulent boundary layer. The Reynolds number based on the momentum thickness of Degraaff & Eaton ($Re_\theta = 2900$) was similar to that in the present study ($Re_\theta = 3050$). This result suggested that the TBL at $X/\delta = 1$ has already been fully developed. This result also indicates that the DBD-PA module itself has nearly no influence on the TBL. As shown in Fig.5, the near-wall region ($y^+ \leq 40$) and the logarithmic region ($40 < y^+ \leq 200$) was determined according to the mean velocity profile. The position of each probe at the nearest point to the wall is not the same, indicating that all the probes are not perfectly in the same plane. However, the maximum height difference between probes in the wall-normal direction is only 0.15 mm, which is about 0.37% of the boundary layer thickness. Therefore, when the experimental results are discussed on a δ scale, the error caused by the height difference between probes could be negligible.

$$\frac{dU^+}{dy^+} = \frac{\frac{(y^+)^2}{\kappa} + \frac{1}{s}}{(y^+)^3 + \frac{(y^+)^2}{\kappa} + \frac{1}{s}} \tag{1}$$

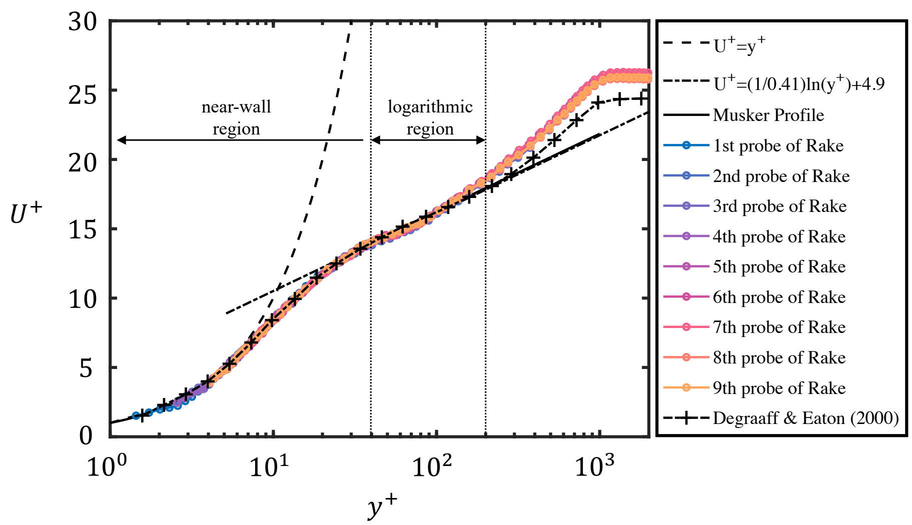

FIG. 5. The mean streamwise velocity profile measured at $X/\delta = 1$ when the DBD-PA was turned off.

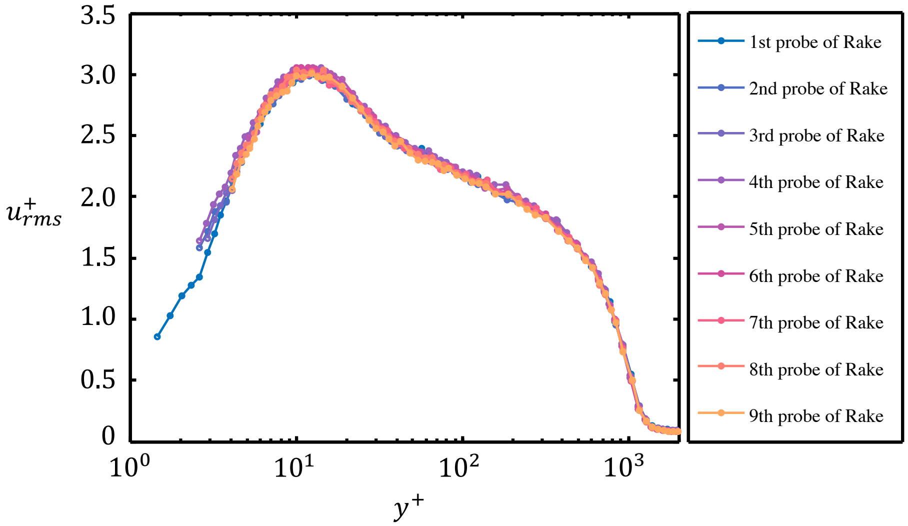

FIG. 6. The root-mean-square streamwise velocity profile measured at $X/\delta = 1$ when the DBD-PA was turned off.

III. CHARACTERISTICS OF ARTIFICIAL VLSMS (AVLSMS)

The distribution of the difference between the low-pass filtered instantaneous velocity when the DBD-PA array was turned on and the mean velocity when it was turned off, as measured by the rake at different heights, are shown in Fig.7 and Fig.8 for the results of $X/\delta = 1$ and $X/\delta = 2$, respectively. The cutoff frequency was $f_{cutoff} = 2\delta/U_{PAOFF}$, where δ is the boundary layer thickness, and U_{PAOFF} was the mean velocity measured when the DBD-PA was turned off. For both streamwise positions, there is a low-speed region that exists for a long time in the middle of the rake, flanked by high-speed regions on both sides. The normalized duration time ($T^+_{AVLSMs} = T_{AVLSMs}U_\infty/\delta$) of these low- and high-speed regions using the freestream velocity U_∞ and boundary layer thickness δ is greater than 10, i.e., $T^+_{AVLSMs} > 10$. As the measurement height increased, these nAVLSMs gradually exhibited meandering characteristics and were occasionally interrupted by pAVLSMs. The meandering of the AVLSMs at a higher position may be attributed to the spanwise velocity components of the counter-rotating streamwise vortices generated by the DBD-PA arrays, as shown in Fig.10, which will be explained later. Moreover, at $X/\delta = 1$, the nAVLSMs (i.e., the blue regions) were more concentrated at the center of the rake at $y/\delta = 0.01$ than at $X/\delta = 2$. This result suggests that the AVLSMs in the near-wall regions became weaker as the streamwise distance increased.

To calculate the averaged width in the spanwise direction of these AVLSMs, the AVLSMs were recognized by choosing the regions where $|(u-\bar{U}_{PAOFF})_L| > KU_\infty$. Here, KU_∞ is the threshold value. In the present study, three different threshold values, i.e., $0.001U_\infty$, $0.005U_\infty$ and $0.01U_\infty$, were used. An example of the recognized AVLSMs is the regions framed by solid lines shown in Fig.7 and Fig.8. The averaged width in the z direction of these AVLSMs calculated using the three different threshold values are shown in Fig.9(a) and (b) for the results of $X/\delta = 1$ and $X/\delta = 2$, respectively. Although the averaged width profile of AVLSMs changes with the selected threshold value, the tendency of these profiles is consistent for each structure when measured at the same streamwise position. For the positive structures, its width reaches to the maximum at $y/\delta = 0.02$ for the $X/\delta = 1$ case and $y/\delta = 0.03$ for the $X/\delta = 2$ case, respectively. Beyond this position, its width gradually decreases with the increasing of wall-normal distance until $y/\delta = 0.11$ for $X/\delta = 1$ case and $y/\delta = 0.13$ for $X/\delta = 2$ case, respectively. For the negative structures, its width decreases rapidly and then reaches the minimum at $y/\delta = 0.02$ for the $X/\delta = 1$ case and $y/\delta = 0.03$ for the $X/\delta = 2$ case, respectively. Beyond this position, the width of nAVLSMs gradually increases with the increasing of wall-normal distance until $y/\delta = 0.11$ for $X/\delta = 1$ case and $y/\delta = 0.13$ for $X/\delta = 2$ case, respectively. To compare with the results of natural ones, the width of VLSMs measured at five different heights in logarithmic region by Chen *et al*.[23] was also plotted in Fig.9 (a) and (b). Although the threshold value to detect the AVLSMs adopted in the present study is different from that to detect the VLSMs in Chen *et al*.[23], the width of nAVLSMs is significantly higher than natural nVLSMs, while the width of pAVLSMs is similar to the natural pVLSMs.

To investigate the characteristics of the AVLSMs in more detail, the mean velocity difference profiles between the cases when the DBD-PA was turned on and turned off measured at the two streamwise positions are shown in Fig.10. The right graph is symmetry around the $z/\delta = 0$ axis, while the left one seems to be symmetry around the $z/\delta = -0.05$ axis. This difference might be caused by the misalignment between the center of the plasma actuator array and the hot-wire rake when measured at $X/\delta = 1$. However, since the width of the hot-wire rake (32 mm) is larger than the width of one period of the plasma actuator array (25 mm) in the spanwise direction, the misalignment does not affect our investigation of the characteristics of AVLSMs and their effects on the bursting phenomena in one spanwise period. In both streamwise positions, it can be confirmed that the low-speed region flanked on the two sides by the high-speed region can reach a height of approximately 0.3δ. This result indicates that the jets generated by the DBD-PA array formed large-scale streamwise vortices. In other words, in the region where the velocity direction of these artificial vortices was upward, the low-speed fluid near the wall was blown up and formed the low-speed region. In contrast, in the region where the velocity direction of these artificial vortices was downward, the high-speed fluid from the outer layer was transported near the wall, thus forming the high-speed region. Compared to the case on the left in Fig.10, the magnitude of the high-speed and low-speed regions in the right one weakened. This result indicates that the artificial large-scale vortices weakened when they were transported downstream. Additionally, as the height increased, the width of the low-speed region first contracted and then slowly increased until $y/\delta = 0.3$. The opposite is true for the high-speed regions. Interestingly, this change is not consistent with the change of width of the extracted nAVLSMs as shown in Fig.9. This incoincidence could be caused by the meandering of AVLSMs at the higher position as shown in Fig.7 and Fig.8. Although the flow field is statistically symmetric, the spanwise velocity components of the artificial large-scale streamwise vortices are not always symmetric because the flow field is turbulent. The spanwise fluctuation velocity can drive the AVLSMs to meander and therefore enhance the mixing of the lifted low-momentum fluid with the induced high-momentum external fluid. Therefore, the wide low-speed region at the higher position shown in Fig.10 does not represent the position of nAVLSMs but could be the result of the averaging of nAVLSMs and pAVLSMs.

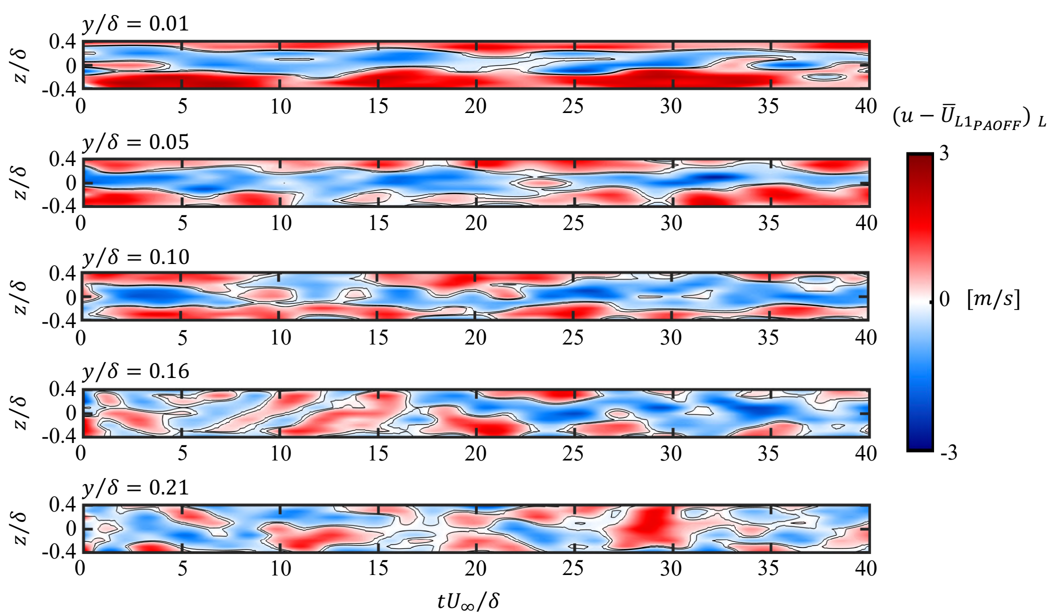

FIG. 7. The distribution of the difference between the instantaneous velocity when DBD-PA array was turned on and the mean velocity when DBD-PA array was turned off measured by rake at different heights. Black contour line: $|(u-\bar{U}_{L1PAOFF})_L| = 0.01U_\infty$. ($X/\delta = 1$)

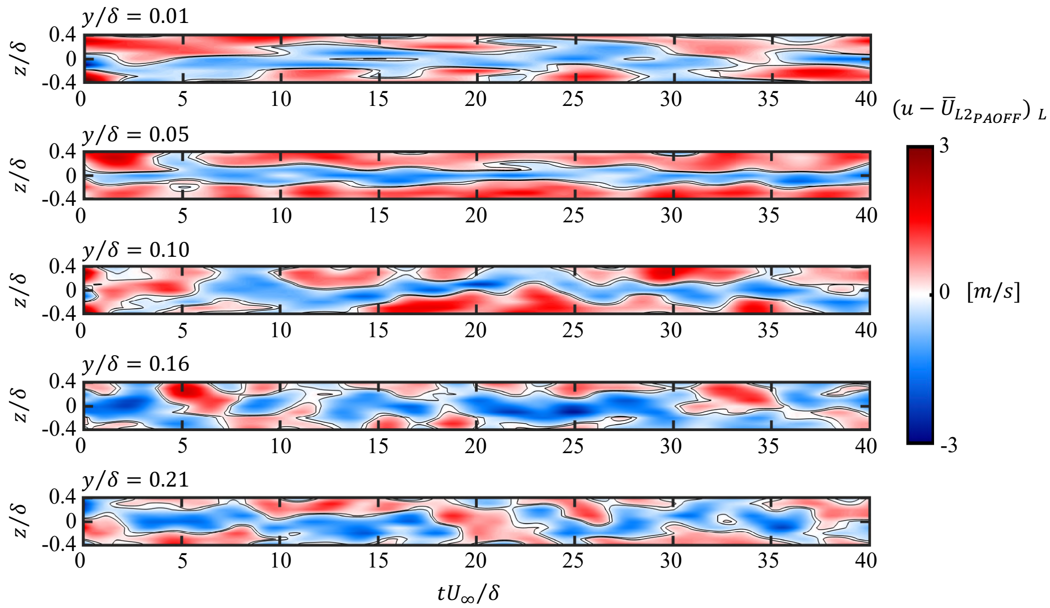

FIG. 8. The distribution of the difference between the instantaneous velocity when DBD-PA array was turned on and the mean velocity when DBD-PA array was turned off measured by rake at different heights. Black contour line: $|(u-\bar{U}_{L2PAOFF})_L| = 0.01U_\infty$. ($X/\delta = 2$)

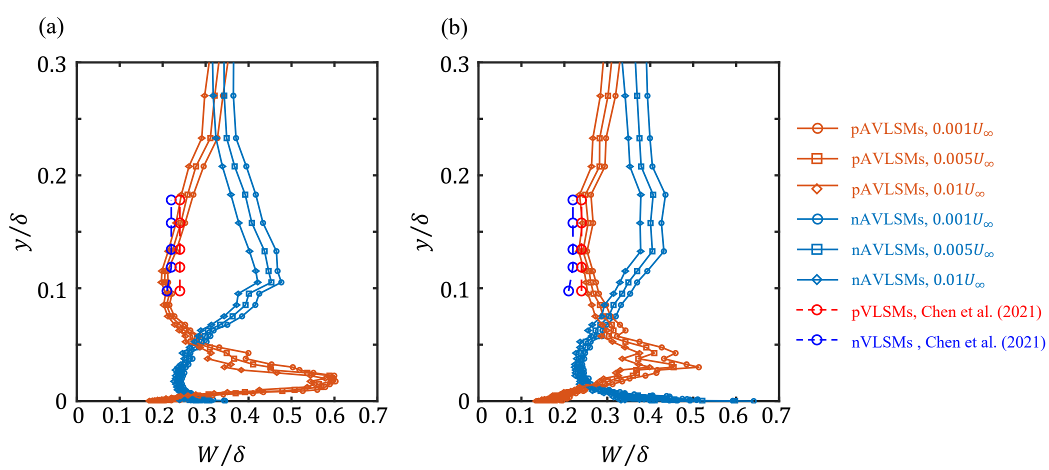

FIG. 9. The averaged width of the recognized AVLSMs using different threshold values: (a) results of $X/\delta = 1$; (b) results of $X/\delta = 2$.

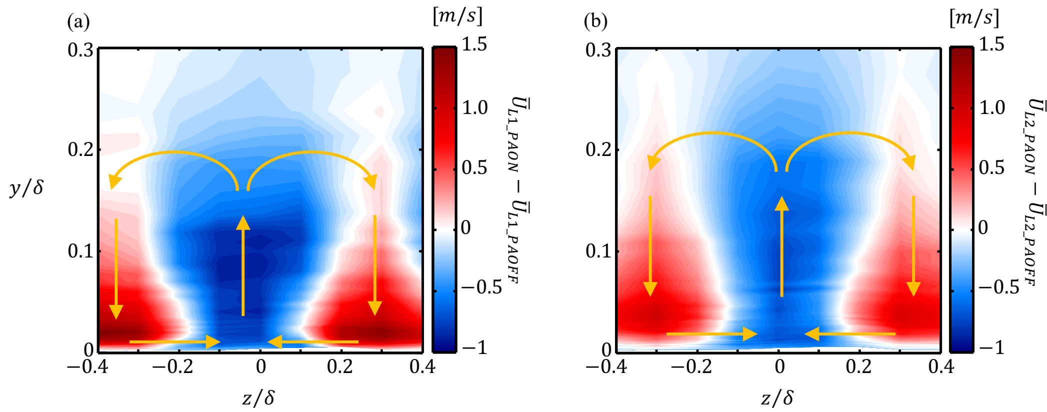

FIG. 10. The mean velocity difference profile: (a) measured at $X/\delta = 1$; (b) measured at $X/\delta = 2$.

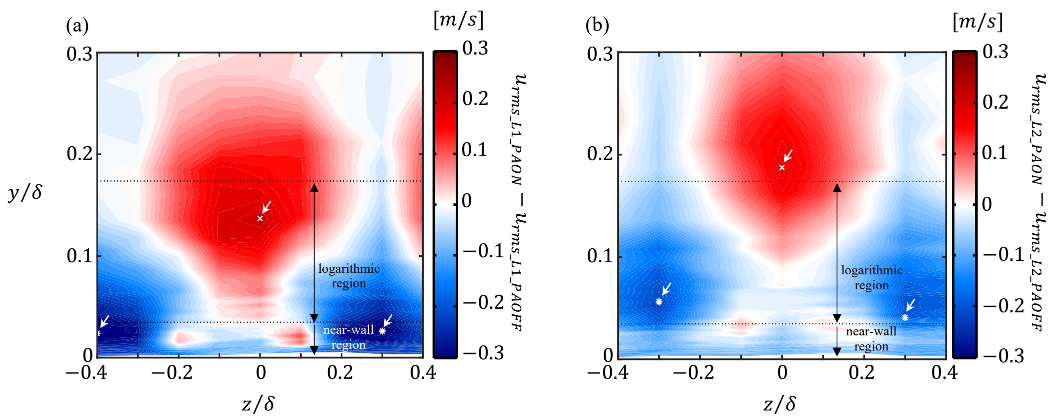

FIG. 11. The turbulent intensity difference profile: (a) measured at $X/\delta = 1$; (b) measured at $X/\delta = 2$. $\times$: local maximum value; $\ast$: local minimum value.

IV. EFFECT OF AVLSMS ON TURBULENT INTENSITY

The turbulent intensity difference profiles between the cases when the DBD-PA was turned on and turned off, measured at the two streamwise positions, are shown in Fig.11. Note that the near-wall and logarithmic regions, separated by dotted lines in Fig.11, were estimated when the DBD-PA was turned off as shown in Fig.5 in section II. By comparing these results with the mean velocity difference profiles shown in Fig.10, it can be found that turbulent intensity does not change significantly in the low-speed regions at the range of $y/\delta \leq 0.05$ for $X/\delta = 1$ and $y/\delta \leq 0.1$ for $X/\delta = 2$; however, it increases at the higher positions, i.e., the red regions in Fig.11. In high-speed regions, the turbulence intensity decreases significantly. Similar results were observed by Yao *et al*.[34] and Cheng *et al*.[27]. The change in turbulent intensity in the present case was completely different from that in the natural LSMs or VLSMs case. In the near-wall region in the natural TBL, the turbulent intensity increases under high-speed large-scale structures but decreases under low-speed structures owing to the modulation effect of LSMs and VLSMs. In the logarithmic region of a natural TBL, the turbulent intensity does not change significantly inside large-scale structures but increases or decreases at the backsides of low-speed/high-speed large-scale structures, owing to the enhancement of hairpin vortices[35]. In the present case, the change in the turbulent intensity in the near-wall and logarithmic regions can be explained as follows. The near-wall high-turbulent fluid flow is lifted up by the counter-rotating artificial large-scale streamwise vortices, and low-speed regions are formed, whereas the flow with low turbulence from the outer region is transported into the near-wall region by the artificial vortices, and high-speed regions are formed.

Additionally, it was observed that the positions of both the maximum (represented by $\times$) and minimum values (represented by $\ast$) in the turbulent intensity difference profile measured at $X/\delta = 2$ (Fig.11 (b)) are higher than those measured at $X/\delta = 1$ (Fig.11 (a)). This result indicates that the overall position of the large-scale artificial vortex generated by the DBD-PA array moves upward with an increase in the streamwise distance from the DBD-PA array. Furthermore, compared to Fig.11 (a), the magnitude of the maximum and minimum values in Fig.11 (b) decreased, suggesting that the large-scale artificial vortex weakens with the increasing streamwise distance from the DBD-PA array.

Further investigation of the effect of AVLSMs on the fluctuation energy of turbulence was performed by calculating the pre-multiplied power spectrum of the streamwise fluctuation velocity measured by the rake. The results for the natural TBL case measured at $X/\delta = 1$ are shown in Fig.12. The result measured at $X/\delta = 2$ when the DBD-PA was turned off was confirmed to be similar and is therefore not shown here. The inner energetic peak, which is due to the near-wall cycle of low-speed streaks and QSVs, can be clearly identified, whereas the outer peak is absent because of the insufficient Reynolds number[6]. Nevertheless, this does not mean that VLSMs did not exist in the present study. The elongated low- and high-speed regions that are longer than 3δ in the streamwise direction can be easily observed from the fluctuation velocity distributions measured in the logarithmic region, as shown in Fig. 10 in our previous study[23].

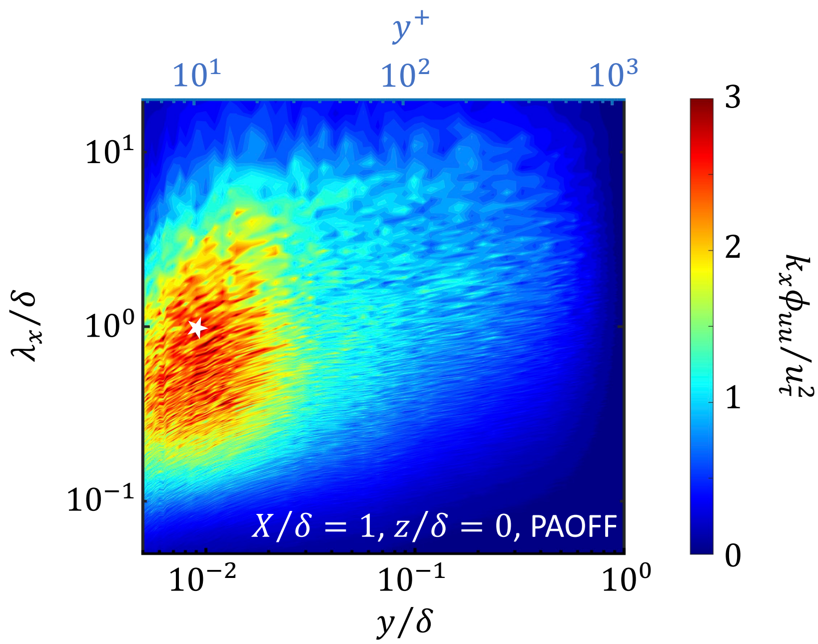

FIG. 12. Pre-multiplied power spectrum of the streamwise fluctuation velocity measured at $X/\delta = 1$ and $z/\delta = 0$ when the DBD-PA was turned off. White star: inner peak.

The pre-multiplied power spectra of the two spanwise positions measured at $X/\delta = 1$ and $X/\delta = 2$ by the rake when the DBD-PA array was turned on are shown in Fig.13. The inner peaks are denoted by black stars, while the outer peaks are denoted by red stars. To compare with the natural TBL case, the inner peak of the natural TBL case is also plotted in Fig.13, which is denoted by the white stars. It can be found that the wall-normal position of the inner peak when DBD-PA was turned on does not change significantly when measured at $X/\delta = 1$, while it becomes higher when measured at $X/\delta = 2$. This result suggests that the structures related to the near-wall cycle have been transported to a higher position together with the AVLSMs at $X/\delta = 2$. In addition, the wavelength of the inner peak becomes smaller significantly when measured at $z/\delta = 0$, suggesting that the streamwise length of the structures related to the near-wall cycle becomes shorter under nAVLSMs. Moreover, the fluctuation energy in the near-wall region in the nAVLSMs, i.e., the $z/\delta = 0$ in Fig.13, does not change significantly. However, in pAVLSMs, i.e., at $z/\delta = 0.4$, the fluctuation energy in the near-wall region was substantially suppressed at $X/\delta = 1$ but returned to a high level at $X/\delta = 2$. This can be explained as follows: At $X/\delta = 1$, the high-speed fluid flow transported from the outer region is at a low-turbulent level, which caused a partial laminarization of the boundary layer. And the boundary layer was developing into a turbulent state downstream of $X/\delta = 1$. Therefore, the fluctuation energy in the near-wall region at $X/\delta = 2$ reached a high level. Moreover, the outer energetic peak (denoted by the red star in Fig.13) with a wavelength of $\lambda_x/\delta \approx 2$ appeared in the logarithmic region in all the four cases, and the fluctuation energy of the outer peaks in Fig.13 (a) and (c) are significantly larger than that of Fig.13 (b) and (d), respectively. These outer peaks might have been caused by the AVLSMs, and the enhanced magnitude of the Fig.13 (a) and (c) cases was considered to be caused by the lifted near-wall low-speed streaks and QSVs. The reasons for this are discussed in the next section.

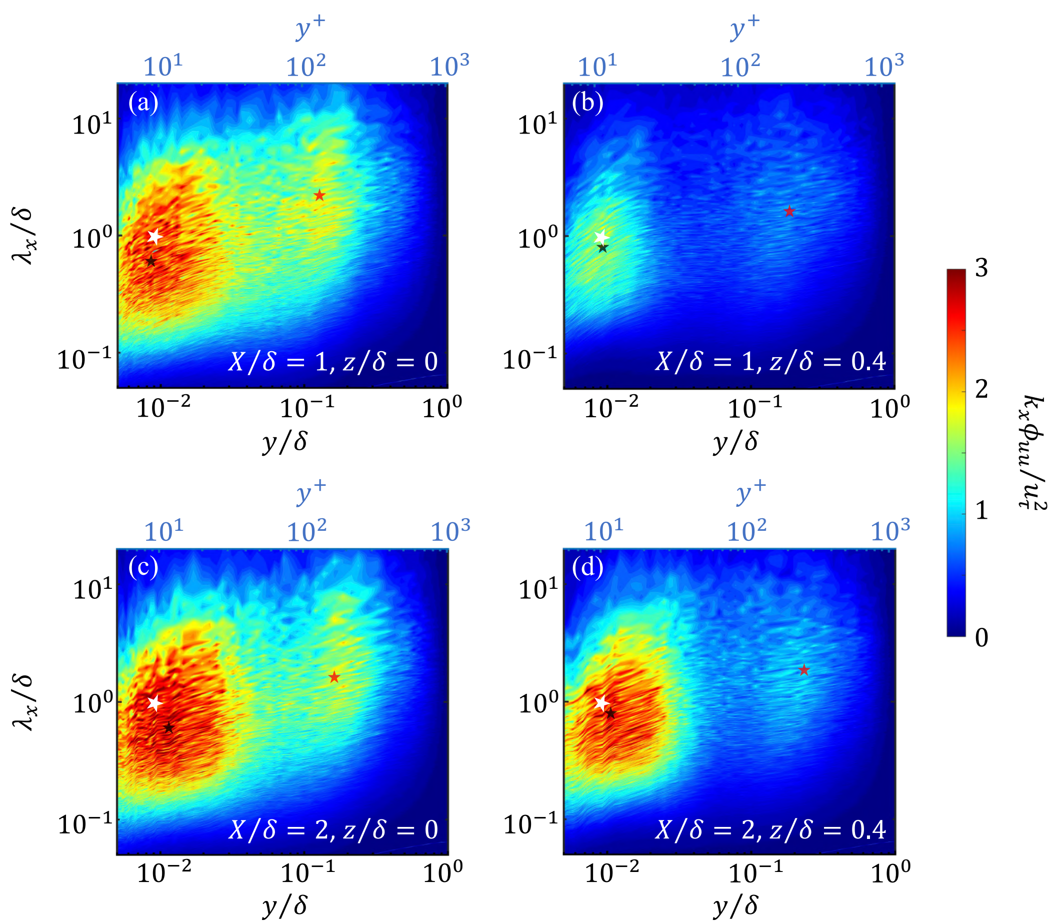

FIG. 13. Pre-multiplied power spectra of the streamwise fluctuation velocity when the DBD-PA was turned on: (a) measured at $X/\delta = 1$ and $z/\delta = 0$; (b) measured at $X/\delta = 1$ and $z/\delta = 0.4$; (c) measured at $X/\delta = 2$ and $z/\delta = 0$; (d) measured at $X/\delta = 2$ and $z/\delta = 0.4$. Black star: inner peak; red star: outer peak; White star: inner peak of the natural TBL case.

V. EFFECT OF AVLSMS ON BURSTING PHENOMENON

To investigate the effect of AVLSMs on the near-wall bursting phenomenon, the bursting frequency in the near-wall region under different conditions was calculated using the variable interval time averaging (VITA) technique. Both the QSV and hairpin vortex can alter the VITA events in the near-wall and logarithmic regions in a natural TBL, respectively,[36–38]. To distinguish their effects, the term "bursting" only refers to the VITA event caused by QSV, whereas the term "VITA event" refers to the one caused by QSV or hairpin vortex in the present study. The VITA technique adopted in the present study was the same as that described by Chen *et al.*[23], in which the normalized time-window is $T^+ = Tu_\tau^2/\nu = 20$ and the detection threshold value is $1.0u_{rms}^2$. It should be noted that the VITA event detection threshold value used in the cases in which the DBD-PA was turned on is the same as that in the case in which it was turned off, so that the detected VITA events would have the same level of strength. As a result, the occurrence frequency difference profiles of the VITA events measured at the two streamwise positions between the cases when the DBD-PA was turned off and turned on are shown in Fig.14. It can be seen that the VITA event frequency increased/decreased in the regions where the mean velocity decreased/increased as shown in Fig.10. This is consistent with the changes in the turbulent intensity, as shown in Fig.11, suggesting that the enhanced outer peak appearing in the pre-multiplied power spectra in Fig.13 (a) and (c) is highly related to these increased VITA events. Although the VITA frequency was not calculated by Cheng *et al.*[27], the strength of the VITA events in the near-wall region was observed to be impaired when the turbulent intensity decreased but was enhanced when the turbulent intensity increased. Therefore, the present results are consistent with those reported by Cheng *et al.*[27].

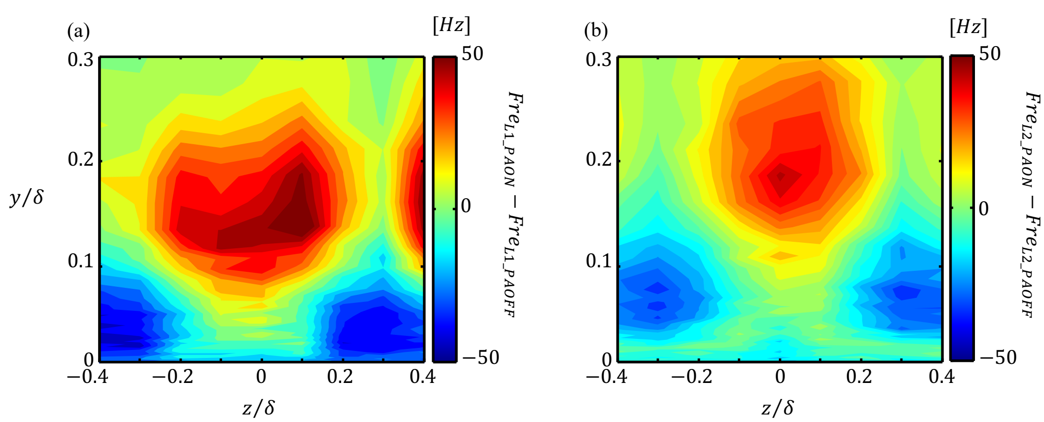

FIG. 14. The VITA event frequency difference profile: (a) measured at $X/\delta = 1$; (b) measured at $X/\delta = 2$.

To investigate the structures related to these increased VITA events in more detail, the ensemble-averaged fluctuation velocity distributions when VITA events were detected by the center probe of the rake in three cases (L1_PAOFF, L1_PAON, L2_PAON) were calculated and are shown in Fig.15. For all these cases, the symmetrical "Y-shape" high-speed region could be confirmed, except for the one measured at $X/\delta = 1$ and $y/\delta = 0.01$ when the DBD-PA was turned on, i.e., the L1_PAON case, which was considered to be caused by the insufficient spanwise resolution of the rake. The distance between the two branches of the "Y-shaped" pattern increased with the distance from the wall, suggesting that the size of the structures related to the detected VITA events also increased with the wall-normal distance. Although the patterns near the walls, i.e., the cases of $y/\delta \leq 0.05$ in Fig.15, are similar to those at higher positions, i.e., the cases of $0.10 \leq y/\delta \leq 0.21$ in Fig.15, the vortices causing them are different. The near-wall VITA events, i.e., the bursting caused by the QSVs, have stronger ejection and sweep than those caused by hairpin vortices at a higher position. In a natural TBL, it is known that the near-wall bursting frequency is significantly higher than the VITA frequency in the logarithmic region (50 Hz vs. 30 Hz) and can be scaled with local inner variables, as described by Chen *et al.*[23]. Moreover, the distance between the high-speed regions, i.e., the branches, in the L1_PAON case, seems to be narrower than that of the L1_PAOFF ones in the range of $0.05 \leq y/\delta \leq 0.15$. The smaller size of the "Y-shape" pattern could be the result of a smaller structure lifted from the near-wall region. However, the size of the "Y-shape" high-speed region in case of L2_PAON does not change significantly when compared to the case of L1_PAOFF. These results support the statement in Section IV, i.e., the outer peak appearing in the pre-multiplied power spectra shown in Fig.13 (a) and (c) was enhanced by the lifted near-wall low-speed streaks and QSVs. We suppose that as these lifted QSVs move downstream, they rapidly deform and develop into large hairpin vortices.

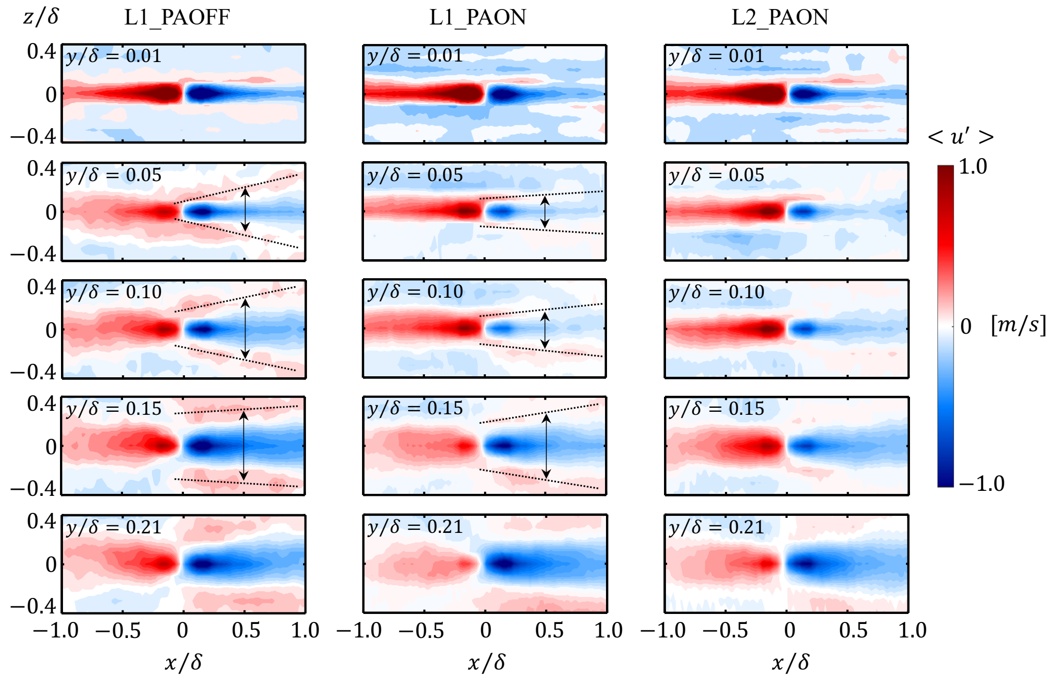

FIG. 15. Ensemble averaged fluctuation velocity distributions when VITA events were detected by the center probe of the rake. Left column: measured at $X/\delta = 1$ when the DBD-PA was turned off; Middle column: measured at $X/\delta = 1$ when the DBD-PA was turned on; Right column: measured at $X/\delta = 2$ when the DBD-PA was turned on.

As discussed by Chen *et al.*[23], in natural TBL, the near-wall bursting frequency is a constant when normalized by the local friction velocity, as suggested by the QSQH theory. The same procedure was performed to verify whether the QSQH theory still holds for artificial large-scale structures. In the procedure, VITA events of each position were re-detected by VITA technique, in which the friction velocity and the R.M.S value measured at the same position were used to calculate the time-window and the detection threshold values. The friction velocity when the DBD-PA was turned on was estimated by fitting the mean velocity profile with a Musker profile in the range of $0 < y^+ \leq 10$ as shown in Fig.16 (a) and (b) for the results measured at $X/\delta = 1$ and $X/\delta = 2$, respectively. For both cases, the mean velocity profile also fits well with the linear sublayer profile, i.e., $U^+ = y^+$, in the range of $0 < y^+ < 7$ as shown in the zoomed graph in Fig.16. This result suggests that the friction velocity was accurately estimated. The spanwise profiles of the friction velocity in four cases (L1_PAOFF, L1_PAON, L2_PAOFF, L2_PAON) are shown in Fig.17. At $X/\delta = 1$, it was found that the friction velocity decreases in the low-speed region and increases in the high-speed region. This tendency is the same as that observed in the natural TBL. However, at $X/\delta = 2$, the friction velocity does not change significantly in the high-speed regions, but decreases in the low-speed regions. Therefore, although the near-wall bursting phenomenon was suppressed under the pAVLSMs at $X/\delta = 1$ as previously mentioned, the skin friction under the pAVLSMs at $X/\delta = 1$ appeared to increase. However, the total skin friction, which was estimated by calculating the mean value of the friction velocity within a range of $-0.31 \leq z/\delta \leq 0.31$ (one period of the DBD-PA array in the spanwise direction), decreased by 0.92% at $X/\delta = 1$ and 4.3% at $X/\delta = 2$. The normalized near-wall bursting frequency $Fre^+ = Fre * \nu/u_\tau^2$ (Fre: bursting frequency), measured at the two streamwise positions, is shown in Fig.18. When measured at $X/\delta = 1$, the bursting frequency is not constant at any wall-normal position, even when it is very close to the wall. However, at $X/\delta = 2$, the bursting frequency became constant at $y/\delta = 0.04$ (approximately under $y^+ = 50$) when normalized with the inner variables. This result can be explained as follows: As mentioned in section IV, at $X/\delta = 1$, the pAVLSMs have transported the low-turbulent flow from the outer region into the near-wall region, which caused a partial laminarization of the boundary layer (see Fig.13 (b)). Therefore, the normalized bursting phenomenon frequency in the high-speed region does not obey the predictions of the QSQH theory. However, at $X/\delta = 2$, the boundary layer has been developed into a higher turbulent level close to that of the fully developed TBL (see Fig.13 (d) and Fig.12). Then, the normalized burst phenomenon frequency in the high-speed region follows the prediction of QSQH theory again. This result suggests that the QSQH theory is valid only when the TBL is sufficiently developed.

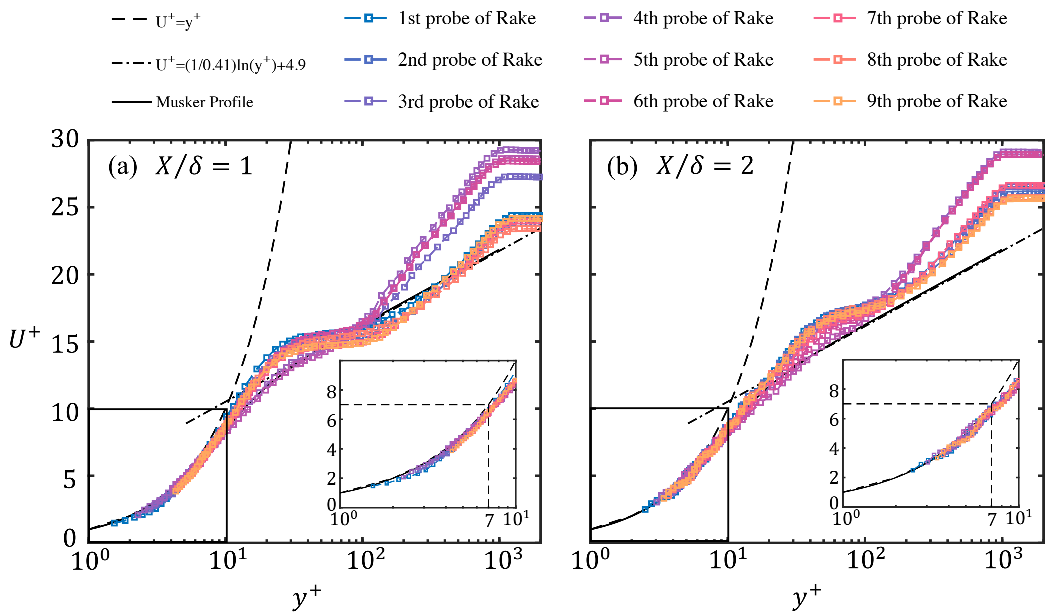

FIG. 16. The mean streamwise velocity profile when PA is turned on: (a) measured at $X/\delta = 1$ and (b) measured at $X/\delta = 2$.

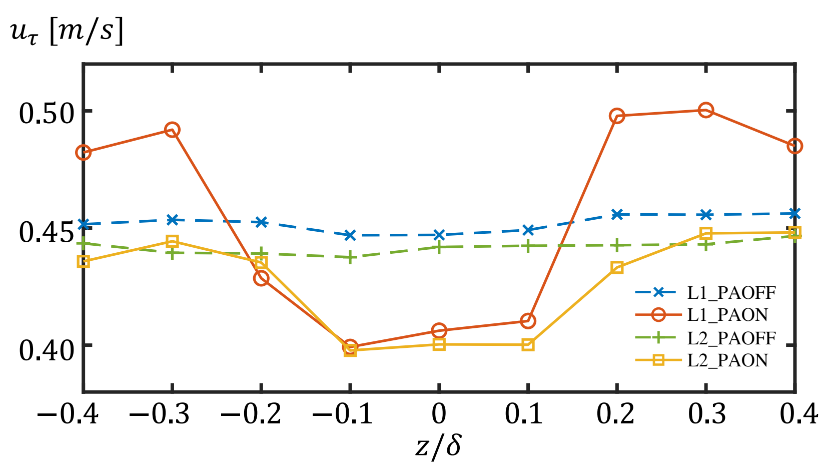

FIG. 17. The spanwise distribution of friction velocity estimated in the four cases. Blue break line: measured at $X/\delta = 1$ when the DBD-PA was turned off; Red solid line: measured at $X/\delta = 1$ when the DBD-PA was turned on; Green break line: measured at $X/\delta = 2$ when the DBD-PA was turned off; Yellow solid line: measured at $X/\delta = 2$ when the DBD-PA was turned on.

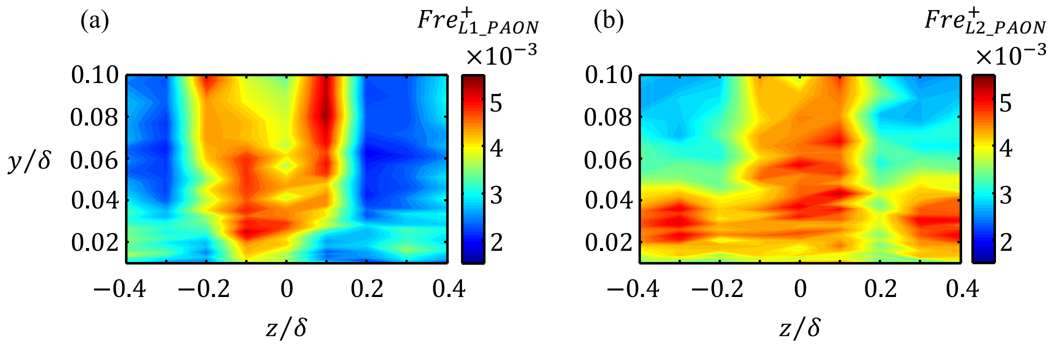

FIG. 18. Normalized bursting frequency profile: (a) measured at $X/\delta = 1$ and (b) measured at $X/\delta = 2$.

VI. CONCLUSION

AVLSMs were successfully created in TBL using a DBD-PA array. In this study, the characteristics of AVLSMs were investigated. The nAVLSM flanked on two sides by pAVLSMs could be detected continuously for a long duration, i.e., $T^+_{AVLSMs} > 10$. The nAVLSM was observed to meander in a higher position. The mean velocity difference between cases in which the DBD-PA was turned on and off suggests that the AVLSM could extend to a height of $y/\delta = 0.3$.

Moreover, the effect of AVLSMs on the turbulent intensity was investigated in detail. The turbulent intensity difference results and the pre-multiplied power spectrum results suggest that the turbulent intensity was suppressed in the pAVLSM, whereas it was increased in the nAVLSMs. This result could be explained by the fact that the pAVLSM transported the outer low-turbulent flow into the near-wall region, and the nAVLSM lifted the near-wall high-turbulent flow to a higher position.

Further investigation indicates that the change in the VITA event frequency in AVLSMs is consistent with the change in turbulent intensity. However, although the near-wall bursting phenomenon was suppressed under the pAVLSMs, the friction velocity increased. Overall, the friction velocity decreased by 0.92% at $X/\delta = 1$ and 4.3% at $X/\delta = 2$. Moreover, it was found that the near-wall bursting frequency normalized by the local inner variables is not uniform under AVLSMs when the turbulence intensity in the pAVLSM shows low values. However, it became the same in the downstream region, where the turbulence in the pAVLSM was developed. This result suggests that the QSQH theory is valid only when the TBL is sufficiently developed.

ACKNOWLEDGMENTS

The present study was partially supported by JSPS KAKENHI (Grants-in-Aid for Scientific Research, Nos. 18K13683 and 20K04264). The authors express their sincere appreciation for the support. They are grateful to Mr. Kouhei Yamaguchi for supporting the experimental setup.

REFERENCES

[1]S. J. Kline, W. C. Reynolds, F. A. Schraub, and P. W. Runstadler, "The structure of turbulent boundary layers," Journal of Fluid Mechanics **30**, 741–773 (1967).

[2]E. R. Corino and R. S. Brodkey, "A visual investigation of the wall region in turbulent flow," Journal of Fluid Mechanics **37**, 1–30 (1969).

[3]S. S. Lu and W. W. Willmarth, "Measurements of the structure of the reynolds stress in a turbulent boundary layer," Journal of Fluid Mechanics **60**, 481–511 (1973).

[4]K. Fukagata, K. Iwamoto, and N. Kasagi, "Contribution of reynolds stress distribution to the skin friction in wall-bounded flows," Physics of Fluids **14**, L73–L76 (2002).

[5]J. Szodruch, "Viscous drag reduction on transport aircraft," in *29th Aerospace Sciences Meeting* (Reno, NV, USA, 1991).

[6]N. Hutchins and I. Marusic, "Evidence of very long meandering features in the logarithmic region of turbulent boundary layers," Journal of Fluid Mechanics **579**, 1–28 (2007).

[7]I. Marusic, R. Mathis, and N. Hutchins, "High reynolds number effects in wall turbulence," International Journal of Heat and Fluid Flow **31**, 418–428 (2010).

[8]A. J. Smits, B. J. McKeon, and I. Marusic, "High–Reynolds Number Wall Turbulence," Annual Review of Fluid Mechanics **43**, 353–375 (2011).

[9]I. Marusic and J. P. Monty, "Attached eddy model of wall turbulence," Annual Review of Fluid Mechanics **51**, 49–74 (2019).

[10]K. C. Kim and R. J. Adrian, "Very large-scale motion in the outer layer," Physics of Fluids **11**, 417–422 (1999).

[11]M. Guala, S. E. Hommema, and R. J. Adrian, "Large-scale and very-large-scale motions in turbulent pipe flow," Journal of Fluid Mechanics **554**, 521–542 (2006).

[12]G. E. Elsinga, R. J. Adrian, B. W. Van Oudheusden, and F. Scarano, "Three-dimensional vortex organization in a high-reynolds-number supersonic turbulent boundary layer," Journal of Fluid

Mechanics **644**, 35–60 (2010).

[13]N. Hutchins, K. Chauhan, I. Marusic, J. Monty, and J. Klewicki, "Towards reconciling the large-scale structure of turbulent boundary layers in the atmosphere and laboratory," Boundary-Layer Meteorology **145**, 273–306 (2012).

[14]Kevin, J. Monty, and N. Hutchins, "The meandering behaviour of large-scale structures in turbulent boundary layers," Journal of Fluid Mechanics **865**, R1 (2019).

[15]G. L. Brown and A. S. Thomas, "Large structure in a turbulent boundary layer," Physics of Fluids **20**, S243–S252 (1977).

[16]P. R. Bandyopadhyay and A. K. Hussain, "The coupling between scales in shear flows," Physics of Fluids **27**, 2221–2228 (1984).

[17]R. Mathis, N. Hutchins, and I. Marusic, "Large-scale amplitude modulation of the small-scale structures in turbulent boundary layers," Journal of Fluid Mechanics **628**, 311–337 (2009).

[18]B. Ganapathisubramani, N. Hutchins, J. P. Monty, D. Chung, and I. Marusic, "Amplitude and frequency modulation in wall turbulence," Journal of Fluid Mechanics **712**, 61–91 (2012).

[19]W. J. Baars, K. M. Talluru, N. Hutchins, and I. Marusic, "Wavelet analysis of wall turbulence to study large-scale modulation of small scales," Experiments in fluids **56**, 1–15 (2015).

[20]S. I. Chernyshenko, I. Marusic, and R. Mathis, "Quasi-steady description of modulation effects in wall turbulence," arXiv:1203.3714 [physics.flu-dyn] (2012).

[21]C. Zhang and S. I. Chernyshenko, "Quasisteady quasihomogeneous description of the scale interactions in near-wall turbulence," Physical Review Fluids **1**, 014401 (2016).

[22]S. I. Chernyshenko, C. Zhang, H. Butt, and M. Beit-Sadi, "A large-scale filter for applications of qsqh theory of scale interactions in near-wall turbulence," Fluid Dynamics Research **51**, 011406 (2019).

[23]X. Chen, K. Iwano, Y. Sakai, and Y. Ito, "Effect of large-scale structures on bursting phenomenon in turbulent boundary layer," International Journal of Heat and Fluid Flow **89**, 108811 (2021).

[24]K. Kevin, J. P. Monty, H. L. Bai, G. Pathikonda, B. Nugroho, J. M. Barros, K. T. Christensen, and N. Hutchins, "Cross-stream stereoscopic particle image velocimetry of a modified turbulent boundary layer over directional surface pattern," Journal of Fluid Mechanics **813**, 412–435 (2017).

[25]Z. Tang, N. Jiang, X. Zheng, and Y. Wu, "Local dynamic perturbation effects on amplitude modulation in turbulent boundary layer flow based on triple decomposition," Physics of Fluids **31**, 025120 (2019).

[26]Z. Tang and N. Jiang, "The effect of a synthetic input on small-scale intermittent bursting events in near-wall turbulence," Physics of Fluids **32**, 015110 (2020).

[27]X. Cheng, C. Wong, F. Hussain, W. Schröder, and Y. Zhou, "Flat plate drag reduction using plasma-generated streamwise vortices," Journal of Fluid Mechanics **918**, A24 (2021).

[28]G. I. Font, "Boundary layer control with atmospheric plasma discharges," AIAA Journal **44**, 1572–1578 (2006).

[29]M. Forte, J. Jolibois, J. Pons, E. Moreau, G. Touchard, and M. Cazalens, "Optimization of a dielectric barrier discharge actuator by stationary and non-stationary measurements of the induced flow velocity: Application to airflow control," Experiments in Fluids **43**, 917–928 (2007).

[30]W. Kim, H. Do, M. G. Mungal, and M. A. Cappelli, "On the role of oxygen in dielectric barrier discharge actuation of aerodynamic flows," Applied Physics Letters **91**, 181501 (2007).

[31]N. Hutchins, T. B. Nickels, I. Marusic, and M. S. Chong, "Hot-wire spatial resolution issues in wall-bounded turbulence," Journal of Fluid Mechanics **635**, 103–136 (2009).

[32]A. J. Musker, "Explicit expression for the smooth wall velocity distribution in a turbulent boundary layer," AIAA Journal **17**, 655–657 (1979).

[33]D. B. Degraaff and J. K. Eaton, "Reynolds-number scaling of the flat-plate turbulent boundary layer," Journal of Fluid Mechanics **422**, 319–346 (2000).

[34]J. Yao, X. Chen, and F. Hussain, "Drag control in wall-bounded turbulent flows via spanwise opposed wall-jet forcing," Journal of Fluid Mechanics **852**, 678–709 (2018).

[35]W. J. Baars, N. Hutchins, and I. Marusic, "Reynolds number trend of hierarchies and scale interactions in turbulent boundary layers," Philosophical Transactions of the Royal Society A: Mathematical, Physical and Engineering Sciences **375**, 20160077 (2017).

[36]R. F. Blackwelder and R. E. Kaplan, "Intermittent structures in turbulent boundary layers," NATO-ACTARD Conf. Proc. **no. 93.** (1972).

[37]R. J. Adrian, C. D. Meinhart, and C. D. Tomkins, "Vortex organization in the outer region of the turbulent boundary layer," Journal of Fluid Mechanics **422**, 1–54 (2000).

[38]R. J. Adrian, "Hairpin vortex organization in wall turbulence," Physics of Fluids **19**, 41301 (2007).